Journal of Solid State Chemistry 184 (2011) 252–263

Contents lists available at ScienceDirect

Journal of Solid State Chemistry

journal homepage: www.elsevier.com/locate/jssc

Synthesis, structure and characterisation of the $n=4$ Aurivillius phase $Bi_5Ti_3CrO_{15}$

A.T. Giddings [a], M.C. Stennett [a], D.P. Reid [a], E.E. McCabe [a,b], C. Greaves [b], N.C. Hyatt [a,*]

[a] Department of Materials Science and Engineering, The University of Sheffield, Mappin Street, Sheffield S1 3JD, UK
[b] School of Chemistry, The University of Birmingham, Edgbaston, Birmingham B15 2 TT, UK

ARTICLE INFO

Article history:
Received 12 July 2010
Received in revised form
17 September 2010
Accepted 22 September 2010
Available online 29 September 2010

Keywords:
Aurivillius
Synthesis
Structure

ABSTRACT

The $n=4$ Aurivillius phase, $Bi_5Ti_3CrO_{15}$, was synthesised by solid state reaction. Rietveld analysis of high resolution neutron diffraction data demonstrated this material to adopt the polar space group $A2_1am$ at room temperature, transforming to the aristotype $I4/mmm$ structure above 650 °C. This phase transition is coincident with an anomaly in DSC signal and relative permittivity, which are characteristic of a ferroelectric–paraelectric phase transition. $Bi_5Ti_3CrO_{15}$ exhibits paramagnetic behaviour at low temperature, with short range antiferromagnetic interactions, but no evidence for long range magnetic ordering. This is considered a consequence of significant disorder of Ti and Cr over the available octahedral sites, as demonstrated by analysis of neutron diffraction data.

1. Introduction

Magnetoelectric multiferroic materials, which display both ferroelectric behaviour and ferromagnetic ordering, are of interest for next generation multiple state memory devices in which binary data is stored in both electric and magnetic polarisation. As pointed out by Hill et al. with the exception of a few notable examples, materials with simultaneous (ferro)magnetic and ferroelectric ordering are rare, as a consequence of the conflicting requirements required to stabilise both ferroic states concurrently [1,2]. One such example is $BiMnO_3$, which adopts a monoclinic distortion of the cubic ABO_3 perovskite structure, where A and B represent large 12-fold and small 6-fold co-ordinate cations, respectively. In typical perovskite ferroelectrics, the spontaneous polarisation in the ferroelectric state is assisted by off-centre displacement of the B-site transition metal cation, stabilised by donation of electron density from filled oxygen $2p$ states into empty transition metal nd states (triggering a second order Jahn Teller distortion). In contrast, the prerequisite for magnetic ordering in perovskites is a superexchange interaction between localised magnetic moments on transition metal cations with partially filled nd states. Thus, in perovskite materials, there is an inherent conflict between stabilisation of ferroelectric and (ferro)magnetic ordering: empty nd states in the former, versus filled nd states in the latter. In the case of $BiMnO_3$, ferromagnetic ordering of Mn^{3+} ($3d^5$) magnetic moments mediated *via* a superexchange interaction is coincident with a ferroelectric distortion arising from off-centre displacement of the Bi cation [1]. The latter is stabilised by covalent Bi–O bonds and the stereoactive Bi $6s^2$ lone pair. Studies of related perovskites have determined antiferromagnetic ordering concomitant with ferroelectric behaviour in $BiFeO_3$ [3], or at least a polar space group at room temperature in $BiCrO_3$ and $BiCoO_3$ [4–6]. However, a complication for device fabrication is that $BiFeO_3$ is known to be metastable at high temperature [7], whereas synthesis of $Bi(Cr,Co)O_3$ requires high pressure conditions (~6 GPa, and 970–1380 °C).

The Aurivillius family of layered perovskites adopt the general formula $Bi_2A_{n-1}B_nO_{3n+3}$, where A is a large 12 co-ordinate cation, and B is a small 6 co-ordinate cation, typically with a d^0 electron configuration [8–10]. In structural terms, such materials may be considered an ordered intergrowth of fluorite-type $[Bi_2O_2]^{2+}$ and perovskite-type $[A_nB_nO_{2n+1}]^{2-}$ layers, forming various homologous series, commonly with $n=1$–4 (e.g. [11–14]). Aurivillius phases typically exhibit ferroelectric behaviour, arising from off-site displacement of A-site and d^0 B-site cations, suggesting potential for multiferroic behaviour if suitable substitution of transition metal cations, with partially filled d-states, could be achieved. Indeed, the co-existence of ferroelectricity and weak ferromagnetism in the $n=4$ Aurivillius phase $Bi_5Ti_3FeO_{15}$, with Fe^{3+} ($3d^5$), has been proposed by several authors [15–17]. The higher homologues $Bi_6Fe_2Ti_3O_{18}$ ($n=5$) and $Bi_9Fe_5Ti_3O_{27}$ ($n=8$) are also reported to show co-existence of ferroelectric and antiferromagnetic ordering, but have not been investigated in detail [17,18]. Several recent studies have demonstrated the potential for doping $n=3$ Aurivillius phases with transition metal

* Corresponding author.
E-mail address: n.c.hyatt@sheffield.ac.uk (N.C. Hyatt).

0022-4596/$ - see front matter © 2010 Elsevier Inc. All rights reserved.
doi:10.1016/j.jssc.2010.09.031

cations having partially filled *d* states. McCabe and Greaves demonstrated spin glass behaviour for $Bi_2Sr_{1.4}La_{0.6}Nb_2MnO_{12}$, with mixed Mn^{3+}/Mn^{4+} ($3d^4/3d^3$), whereas $Bi_2Sr_2Nb_{2.5}Fe_{0.5}O_{12}$, with Fe^{3+} ($3d^5$), exhibited almost ideal Curie–Weiss paramagnetism with short range antiferromagnetic exchange; both compounds adopt the non-polar aristotype *I*4/*mmm* structure [19,20]. Sharma et al. reported ferroelectric behaviour in a family of transition metal substituted Aurivillius phases, formulated $Bi_{2-x}S_{r2+x}(Nb,Ta)_{2+x}M_{1-x}O_{12}$ with $M=Ru^{4+}$ ($4d^4$), Ir^{4+} ($5d^5$), Mn^{4+} ($3d^3$) and $x\approx0.5$; these compounds are paramagnetic with short range ferromagnetic (Mn) or antiferromagnetic (Ru, Ir) exchange [21,22]. $Bi_3Fe_{0.5}Nb_{1.5}O_9$, with Fe^{3+} ($3d^5$), is the only transition metal doped double layer Aurivillius phase known to date, it is reported to be ferroelectric and exhibit Curie–Weiss paramagnetism with short range antiferromagnetic exchange [23]. However, in the absence of evidence for switchable polarisation states in $Bi_3Fe_{0.5}Nb_{1.5}O_9$ (e.g. a polarisation hysteresis loop), this compound should more properly be considered pyroelectric, consistent with the assignment of a polar space group at room temperature.

Clearly, the generic structure of Aurvillius phases has the potential to serve as a template for multiferroic behaviour, with suitable doping and ordering of transition metal cations possessing partially filled *d* states. Since the only definitive example of such an $n=4$ Aurivillius phase is $Bi_5Ti_3FeO_{15}$, we sought to establish the existence of hypothetical analogues $Bi_5Ti_3MO_{15}$ with M=Cr, Mn and Co. Here, we report the synthesis, structure and characterisation of $Bi_5Ti_3CrO_{15}$, this material is ferroelectric but exhibits paramagnetism with short-range antiferromagnetic exchange.

2. Experimental

A polycrystalline sample of $Bi_5Ti_3CrO_{15}$ was prepared by solid state reaction between stoichiometric quantities of Bi_2O_3, TiO_2 and Cr_2O_3. To optimize the synthesis of $Bi_5Ti_3CrO_{15}$, the reaction was monitored by laboratory X-ray diffraction (Stoe STADI-P diffractometer, operating in transmission mode with Cu$K\alpha_1$ radiation and a position sensitive detector). Reagents were intimately mixed and heated for 12 h in air at 800–1000 °C, at intervals of 50 °C with intermittent regrinding. A final annealing step was performed at 1025 °C for 12 h in air, with slow cooling at 2 °C min^{-1} to room temperature. Where high density pellets were required, $Bi_5Ti_3CrO_{15}$ powder was uniaxially pressed into 8 mm pellets which were sintered at 1025 °C for 6 h in air, with slow cooling at 2 °C min^{-1} to room temperature. This afforded pellets with densities in the range 89–93% of theoretical. Elemental analysis was undertaken using a CAMECA SX50 WDS-EPMA, sintered specimens were embedded in cold setting epoxy resin and polished to a finish of 0.25 μm diamond paste prior to analysis. Dielectric measurement was performed on a sintered pellet with Au electrodes, using a Hewlett Packard 4284 A LCR meter from room temperature to 700 °C, at fixed frequencies of 1, 10 and 100 kHz. Differential scanning calorimetry was performed using a Netzsch DSC404C calorimeter. A 40 mg powdered sample was heated to 850 °C and cooled subsequently to room temperature, at a rate of 10 °C min^{-1}. Magnetic measurements were carried out on a Quantum Design Physical Property Measurement System model 6000. Data were acquired using the direct current induction method with a field of 3000 Oe. Field cooled (FC) and zero field cooled (ZFC) data sets were collected from room temperature to 3 K. Cr K-edge X-ray Absorption Spectroscopy data from $Bi_5Ti_3CrO_{15}$ were acquired on beamline X23A2 of the National Synchrotron Light Source (NSLS), Brookhaven National Laboratory (BNL), USA. Data were acquired in transmission mode using finely ground specimens dispersed in BN to achieve a thickness of one absorption length. Data reduction and analysis was performed using the programs Athena and Artemis [24].

Variable temperature time-of-flight neutron powder diffraction data were acquired on the high resolution powder diffractometer (HRPD), at the STFC ISIS Facility, Chilton, UK. A 10 g sample was contained in a 5 mm thick slab-type vanadium can, mounted within a high temperature furnace. For the purpose of structure refinement data collection times were ~6 h in the polar phase at room temperature and ~3 h in the non-polar phase at 700 °C; for the purpose of unit cell parameter refinement, data were also acquired in ~15 min at intermediate temperatures. The diffraction data were normalized to the incident beam spectrum, and corrected for detector efficiency (using a vanadium standard) and sample attenuation. Structure determination was made by Rietveld analysis of neutron diffraction data, using the GSAS suite of programs [25] and data from both the high resolution back scattering detectors (Bank 1: $2\theta\approx168°$, $\Delta d/d=5\times10^{-4}$) and moderate resolution transverse detectors (Bank 2: $2\theta\approx90°$, $\Delta d/d=2\times10^{-3}$).

3. Results

3.1. Synthesis of $Bi_5Ti_3CrO_{15}$

Powder X-ray diffraction revealed the initial products of solid state reaction at 800 °C to be $Bi_4Ti_3O_{12}$ and $Bi_{3.73}Cr_{0.32}O_{6+x}$ (a stabilised form of δ-Bi_2O_3), together with excess Cr_2O_3. Analysis of the product following reaction at higher temperatures showed that these compounds subsequently react to yield $Bi_5Ti_3CrO_{15}$. The overall cation composition determined by EPMA was in accordance with the target stochiometry: Bi 4.99(1), Ti 3.01(2) Cr 1.00(2); note oxygen is not determined accurately using this method and was assumed on the basis of cation stochiometry. The diffraction pattern of the product reacted at 1025 °C (Fig. 1) could be indexed on an $A2_1am$ cell, with unit cell parameters $a=5.454(1)$ Å, $b=5.435(1)$ Å, $c=40.701(9)$ Å, characteristic of an $n=4$ Aurivillius phase (note: non-standard space group settings are used herein for purpose of comparison and continuity with existing literature data where required).

3.2. Synthesis of $Bi_5Ti_3MO_{15}$ where M=Fe, Mn, Co

Synthesis of a number of related transition metal bearing compounds was also attempted, under conditions similar to those

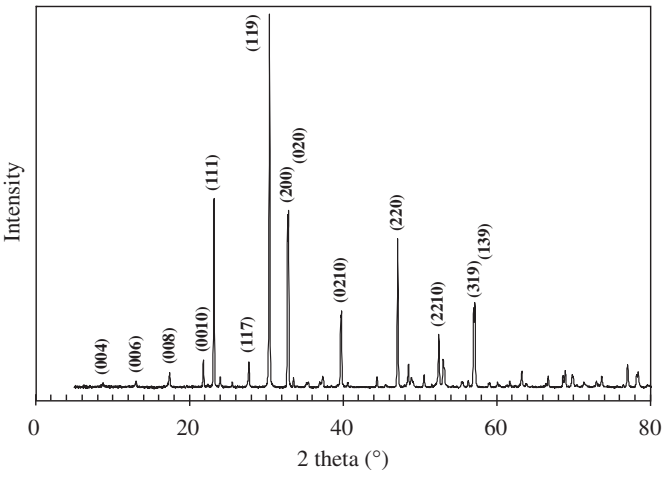

Fig. 1. X-ray diffraction pattern for $Bi_5Ti_3CrO_{15}$ after heating to 1025 °C, indexing of key reflections is shown.

used to synthesise $Bi_5Ti_3CrO_{15}$. The previously reported compound $Bi_5Ti_3FeO_{15}$ was successfully prepared by this method, but we could not synthesise the (hypothetical) compounds $Bi_5Ti_3MnO_{15}$ and $Bi_5Ti_3CoO_{15}$ (with no evidence for a phase with $c\sim40$ Å present in the diffraction patterns, following reaction at 1025 °C).

3.3. Electrical measurements

Fig. 2 shows the temperature dependence of the relative permittivity of $Bi_5Ti_3CrO_{15}$, measured at frequencies of 1, 10 and 100 kHz. At higher frequencies the relative permittivity exhibits a maximum at 660 °C, together with a divergence in the loss tangent (see inset), which are characteristic (but not definitive) of a ferroelectric–paraelectric phase transition. The relative permittivity increases at higher temperatures as a consequence of the conductivity of the specimen; similar behaviour was previously observed in a wide range of known ferroelectric Aurivillius phases [26]. Unfortunately, the conductivity of sintered $Bi_5Ti_3CrO_{15}$ prevented the measurement of a saturated hysteresis loop at room temperature and we are therefore unable to conclude with absolute certainty that the anomaly in permittivity observed at 660 °C is associated with a ferroelectric–paraelectric phase transition. However, such an assignment would be consistent with both the room temperature polar structure and high temperature phase transitions of $Bi_5Ti_3CrO_{15}$ reported in subsequent sections, and the observed dependence of Curie temperature on estimated spontaneous polarisation in this class of compounds, as discussed later.

3.4. Differential scanning calorimetry

The DSC traces on heating and cooling of $Bi_5Ti_3CrO_{15}$ (to 850 °C) are shown in Fig. 3. On heating, an initial endothermic rise and fall was observed at low temperature; this is typical of DSC curves at low temperature and not representative of any structural change. After this period, the DSC signal exhibited a steady rise until a sharp endothermic anomaly was observed which peaked at 660 °C. No further anomalies were exhibited up to 850 °C. On cooling, a sharp exothermic anomaly was observed at 660 °C, indicating a fully reversible phase transition. The temperature of this phase transition is consistent with that determined by electrical and neutron diffraction methods, as discussed in Sections 3.3 and 3.7. The sharp nature of the observed DSC anomaly is typical of a first-order structural phase transition [27]. The related phase $Bi_5Ti_3FeO_{15}$ is known to exhibit a similar first-order transition, between ferroelectric and paraelectric

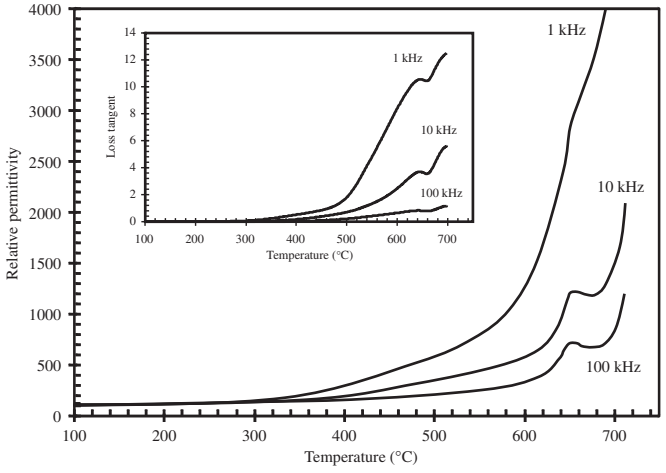

Fig. 2. Temperature dependence of relative permittivity and loss tangent of $Bi_5Ti_3CrO_{15}$.

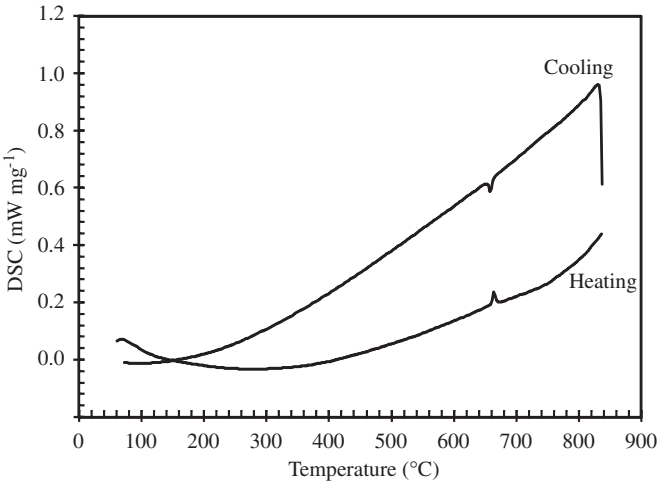

Fig. 3. Temperature dependence of DSC response from $Bi_5Ti_3CrO_{15}$, an anomaly indicative of a structural phase transition is observed at $T=660$ °C.

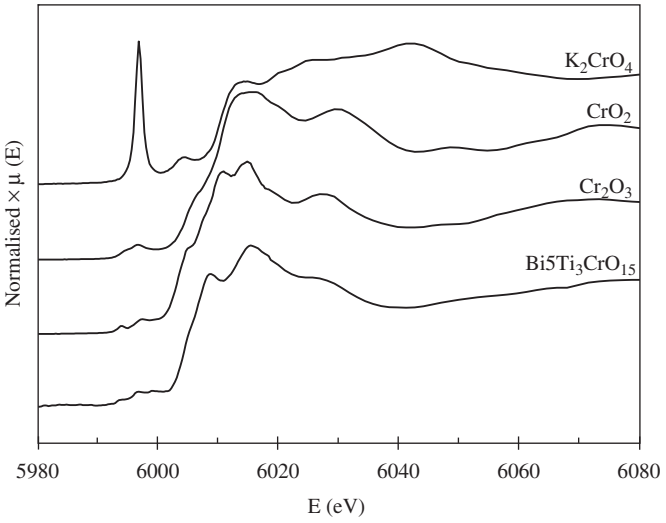

Fig. 4. Cr K-edge XANES spectra of $Bi_5Ti_3CrO_{15}$, Cr_2O_3, CrO_2, and K_2CrO_4.

structures, at $T_c=730$ °C [14]. Although Snedden et al. were unable to detect such a phase transition in $Bi_5Ti_3FeO_{15}$ using DTA or DSC methods, we observed a strong DSC anomaly at ~730 °C, similar to that observed for $Bi_5Ti_3CrO_{15}$. This gives credence to the electrical and structural data presented here for $Bi_5Ti_3CrO_{15}$, which are consistent with a ferroelectric–paraelectric phase transition at 660 °C.

3.5. Cr K-edge X-ray absorption spectroscopy

Analysis of Cr K-edge XANES spectra has been applied for "finger print" identification and quantification of Cr species in a diverse range of materials, including Lunar basalts [28], soils [29], and microbes [30]. Fig. 4 shows the Cr K-edge XANES spectra of several well characterised standard compounds together with that of $Bi_5Ti_3CrO_{15}$. The spectra and edge positions determined from the first derivative are in good agreement with those published previously [31–33]. The absorption edge (E_0) is observed to shift to higher energy with increasing oxidation state, by ~1 eV per unit of charge, as shown in Table 1 and in agreement with previous studies [28,31]. This reflects the increased binding energy of the K-shell photoelectron with increasing oxidation state of the Cr absorber atom. Table 1 shows

Table 1
Absorption edge energy determined from first derivative of Cr K-edge XANES spectra for various oxidation states.

Compound	Oxidation state	Co-ordination	E_0 (eV)
Cr_2O_3	+3	Octahedral	6006.7 ± 0.3
$Bi_5Ti_3CrO_{15}$	+3	Octahedral	6007.0 ± 0.3
CrO_2	+4	Octahedral	6008.5 ± 0.3
K_2CrO_4	+6	Tetrahedral	6010.2 ± 0.3

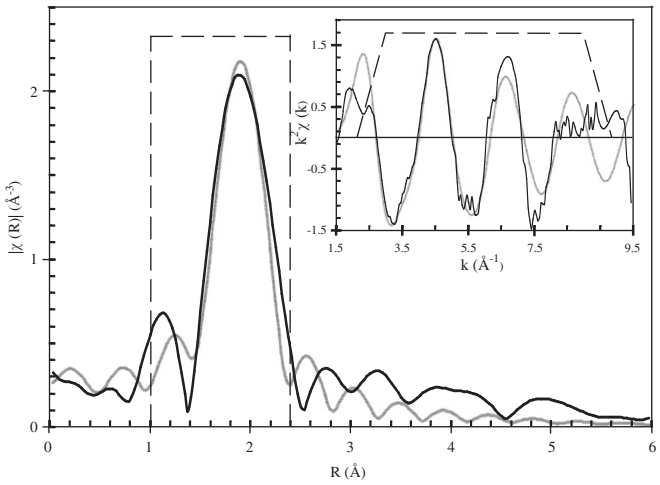

Fig. 5. Fit (grey line) to Fourier transform of Cr K-edge EXAFS data (black line) from $Bi_5Ti_3CrO_{15}$, based on simplified *I*4/*mmm* model (see text); inset shows measured (black line) and calculated (grey line) $k^2\chi(k)$ data. Fit parameters: $S_0^2 = 0.8 \pm 0.2$, $E_0 = -3.0 \pm 0.8$ eV; for four variables against 8.7 independent data points. The *R*-factor was 5.4%.

the absorption edge energies of Cr_2O_3 and $Bi_5Ti_3CrO_{15}$ to be identical, within precision, consistent with the presence of octahedral Cr^{3+} in $Bi_5Ti_3CrO_{15}$. The XANES spectrum of K_2CrO_4 shows an intense pre-edge feature at $E = 5997.0 \pm 0.3$ eV, which is well known to be associated with a $1s \rightarrow 3d$ transition between bound electronic states [34]. This transition is forbidden by the dipole selection rule, $\Delta l = \pm 1$, for electronic transitions. However, the selection rule is relaxed in the case of metal 3*d* and oxygen 2*p* orbital hybridisation in a non-centrosymmetric (e.g. tetrahedral) co-ordination environment. In the case of $Bi_5Ti_3CrO_{15}$, Cr_2O_3, and CrO_2, this feature is weak, and indicative of only rather small distortion from ideal octahedral symmetry. This is consistent with structure refinement of $Bi_5Ti_3CrO_{15}$ based on neutron diffraction data, as discussed in the next section, and the known crystal structures of CrO_2 and Cr_2O_3 [35,36].

Analysis of Cr K-edge Extended X-ray absorption fine structure (EXAFS) data, (Fig. 5), confirmed the presence of octahedral Cr^{3+} in $Bi_5Ti_3CrO_{15}$. A model based on the crystal structure presented in Section 3.6, was used to fit the EXAFS data; assuming full Cr occupation of the inner Ti/Cr1 site by Cr (see Section 3.6). The Fourier transform of the EXAFS data shows a strong signal at $R \approx 2.0$ Å, associated with the nearest neighbour Cr–O distance (Fig. 5). The EXAFS data and Fourier transform could be adequately modelled with a single Cr–O contact distance of 1.94 ± 0.2 Å, which is in reasonable agreement with the weighted mean average Cr–O distance of 1.98 Å determined by neutron diffraction (see Section 3.6). The mean squared displacement parameter refined for the Cr–O path, $\sigma^2 = 0.012 \pm 0.004$ Å, signifies considerable (positional and thermal) disorder. This is a likely consequence of using only a single Cr–O distance to model the spread of inequivalent bond lengths associated with two

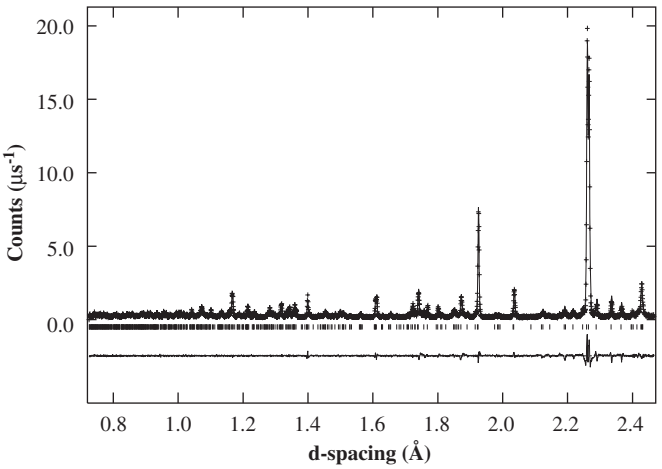

Fig. 6. Showing fit (solid line) to high resolution (Bank 1, $2\theta \approx 168^\circ$) neutron diffraction data (points) for $Bi_5Ti_3CrO_{15}$ at 25 °C in space group $A2_1am$; tick marks show allowed reflections, the difference profile (lower solid line) demonstrates an excellent fit to the data.

different crystallographic sites, present in the real structure, as discussed in Section 3.6.

3.6. Crystal structure of $Bi_5Ti_3CrO_{15}$ at 25 °C

Preliminary analysis of room temperature (25 °C) diffraction data assumed $Bi_5Ti_3CrO_{15}$ to be isostructural with the $n=4$ Aurivillius phases $Bi_4ATi_4O_{15}$ and $Bi_5Ti_3FeO_{15}$ (A=Ba, Sr, Ca, Pb), which all adopt space group $A2_1am$ [37–40]. Structure refinement at 25 °C allowed for disorder of Ti and Cr over the two unique octahedral sites in the perovskite type layer, since the contrast in neutron scattering lengths between Ti (−3.438 fm) and Cr (3.635 fm), allows (in principle) accurate determination of site occupancy. The co-ordinates and thermal parameters of the Ti and Cr atoms adopting the same cation site were constrained to be equal, and site occupancies were constrained to sum to unity (subject to the nominal composition of the sample). Refinement of a model in space group $A2_1am$ proceeded smoothly (total of 70 variables, with 54 structural parameters), yielding an excellent final fit to the diffraction data as shown in Fig. 6; the refined structural parameters are given in Table 2, key bond lengths are summarised in Table 3, and cation bond valence sums are given in Table 4 [41]. The crystal structure of $Bi_5Ti_3CrO_{15}$ is shown schematically in Fig. 7. Ti and Cr were found to preferentially occupy the outer Ti/Cr2 and inner Ti/Cr1 sites, respectively, as discussed in Section 4.3. The final combined agreement indices were $\chi^2 = 4.09$, $R_{wp} = 9.92$, and $R_p = 9.20$. Refinement of a model in space group *Amam*, which permits the same co-operative octahedral tilt pattern as $A2_1am$ but without polar displacements, yielded physically unrealistic thermal parameters for several atoms and so was rejected. Thus, $Bi_5Ti_3CrO_{15}$ was confirmed to be isostructural with $Bi_4ATi_4O_{15}$ and $Bi_5Ti_3FeO_{15}$ (A=Ba, Sr, Ca, Pb) at room temperature [37–40].

3.7. High temperature structure and phase transition of $Bi_5Ti_3CrO_{15}$

To determine the possible high temperature structure(s) of $Bi_5Ti_3CrO_{15}$, it was useful to consider the Group–sub–group relations connecting the aristotype *I*4/*mmm* and $A2_1am$ structures by symmetry breaking distortions. This is conveniently achieved using the program "Subgroupgraph" available on the Bilbao Crystallographic Server [42]. Using common non-standard settings, Fig. 8 shows there are three possible intermediate

Table 2
Refined structural parameters for $Bi_5Ti_3CrO_{15}$ at 25 °C.

Space group: $A2_1am$		$a=5.45422(8)$ Å	$b=5.43574(7)$ Å	$c=40.70171(57)$ Å	
Atom	**Pos.**	***x***	***y***	***z***	**U_{iso} (×100) Å²**
Bi1	4*a*	0.25[a]	0.248(1)	0	1.2(1)
Bi2	8*b*	0.241(3)	0.252(1)	0.10313(9)	2.4(1)
Bi3	8*b*	0.236(2)	0.268(1)	0.21805(9)	2.3(1)
Ti/Cr1[b]	8*b*	0.272(8)	0.239(8)	0.4476(7)	0.5(2)
Ti/Cr2[c]	8*b*	0.286(4)	0.244(2)	0.3487(2)	0.6(2)
O1	4*a*	0.317(2)	0.191(2)	0.5	0.1(3)
O2	8*b*	0.589(2)	0.530(1)	0.0519(1)	1.5(2)
O3	8*b*	0.323(2)	0.307(1)	0.4030(1)	1.1(2)
O4	8*b*	0.520(2)	0.481(1)	0.1375(1)	2.0(2)
O5	8*b*	0.283(3)	0.198(1)	0.3057(1)	2.8(2)
O6	8*b*	0.516(2)	0.488(1)	0.2491(2)	3.0(2)
O7	8*b*	0.029(3)	−0.026(1)	0.0414(1)	1.6(2)
O8	8*b*	0.076(2)	0.027(2)	0.1514(1)	3.00(3)
	Bank		**R_{wp} (%)**	**R_p (%)**	
Powder statistics	1		12.90	11.45	
	2		8.78	7.07	
	Combined		9.92	9.20	$\chi^2=4.09\%$

[a] Co-ordinate fixed to define origin of polar axis.
[b] Ti/Cr site occupancy 0.629/0.371(8), co-ordinates and U_{iso} constrained to be equal, site occupancy constrained to unity.
[c] Ti/Cr site occupancy 0.871/0.129(8), co-ordinates and U_{iso} constrained to be equal, site occupancy constrained to unity.

Table 3
Bond lengths determined from Rietveld analysis of neutron diffraction data for $Bi_5Ti_3CrO_{15}$ at 25 °C.

Bond length (Å)		**Bond length (Å)**	
Bi1-O1	2.436(14)	Ti/Cr1–O1	2.161(29)
	2.383(15)	Ti/Cr1–O2	1.77(6)
	3.050(13)		2.07(5)
	3.111(14)	Ti/Cr1–O3	1.874(32)
Bi1–O2	2.583(10) × 2	Ti/Cr1–O7	2.15(5)
	3.202(11) × 2		1.89(6)
Bi1–O7	2.573(14) × 2		
	2.553(13) × 2	Ti/Cr2–O3	2.248(10)
		Ti/Cr2–O4	1.979(18)
Bi2–O2	2.534(9)		1.998(18)
	3.198(9)	Ti/Cr2–O5	1.766(9)
Bi2–O3	2.316(1)	Ti/Cr2–O8	2.008(19)
	3.202(11)		1.920(19)
	2.474(11)		
	3.059(11)		
Bi2–O4	2.413(11)		
	2.346(12)		
Bi2–O7	3.154(10)		
	3.207(10)		
Bi2–O8	2.484(11)		
	3.083(12)		
Bi3–O5	2.657(14)		
	3.145(15)		
	3.256(10)		
	2.544(10)		
	2.318(12)		
	2.185(12)		
	2.273(12)		
	2.539(12)		

Table 4
Cation bond valence sums, calculated at room temperature according to the scheme of Brown and Altermatt [41].

Cation	**Bond valence sum (v.u.)**
Bi1	2.78
Bi2	2.84
Bi3	2.92
Ti1	4.09
Cr1	3.20
Ti2	4.05
Cr2	3.17

structures, with symmetry *F2mm*, *Amam* and *Abam*, connecting $A2_1am$ and *I4/mmm* through a common *Fmmm* structure. Therefore, $Bi_5Ti_3CrO_{15}$ could be expected to transform to the aristotype *I4/mmm* structure *via* either polar (*F2mm*) or non-polar (*Amam* or *Abab*) intermediate structures, in a sequence of continuous phase transitions.

Inspection of neutron diffraction data up to 650 °C, showed the presence of weak *h k l* reflections with $h+l\neq 2n$ which are not permitted by space group *F2mm*. For example, Fig. 9 shows the presence of (1 2 8), (1 2 6), (2 1 5) and (1 2 4) reflections at 650 °C, located at $d=2.21$, 2.31, 2.35, and 2.28 Å; these reflections are permitted in $A2_1am$ but not *F2mm*. Although we cannot rule out a transformation from polar $A2_1am$ to polar *F2mm* structures above 650 °C, the temperature window of such a hypothetical phase must be less than 10 °C, assuming a Curie temperature of 660 °C. On the basis of the available data, we conclude that the structure of $Bi_5Ti_3CrO_{15}$ adopts space group $A2_1am$ from 25 °C up to 660 °C.

Diffraction data acquired at 670 °C could be indexed in space group *I4/mmm*. Comparison of Figs. 9 and 10 shows the absence of *h k l* reflections with $k+l=2n$ at 670 °C, which are characteristic of $A2_1am$, *Amam* and *Abam* symmetry. Thus, neutron diffraction data suggest a discontinuous transition from a polar $A2_1am$ to non-polar aristotype *I4/mmm* structure at 660 °C. The temperature window of any hypothetical *Amam* or *Abam* intermediate phase must therefore be exceedingly small and less than 10 °C.

Diffraction data acquired in the range 100–670 °C were not of sufficient statistical quality to permit full Rietveld analysis, but allowed the unambiguous observation of key reflections to permit determination of space group symmetry, as described above. However, unit cell parameters could be determined from these diffraction data, by profile fitting using the Le Bail method, as

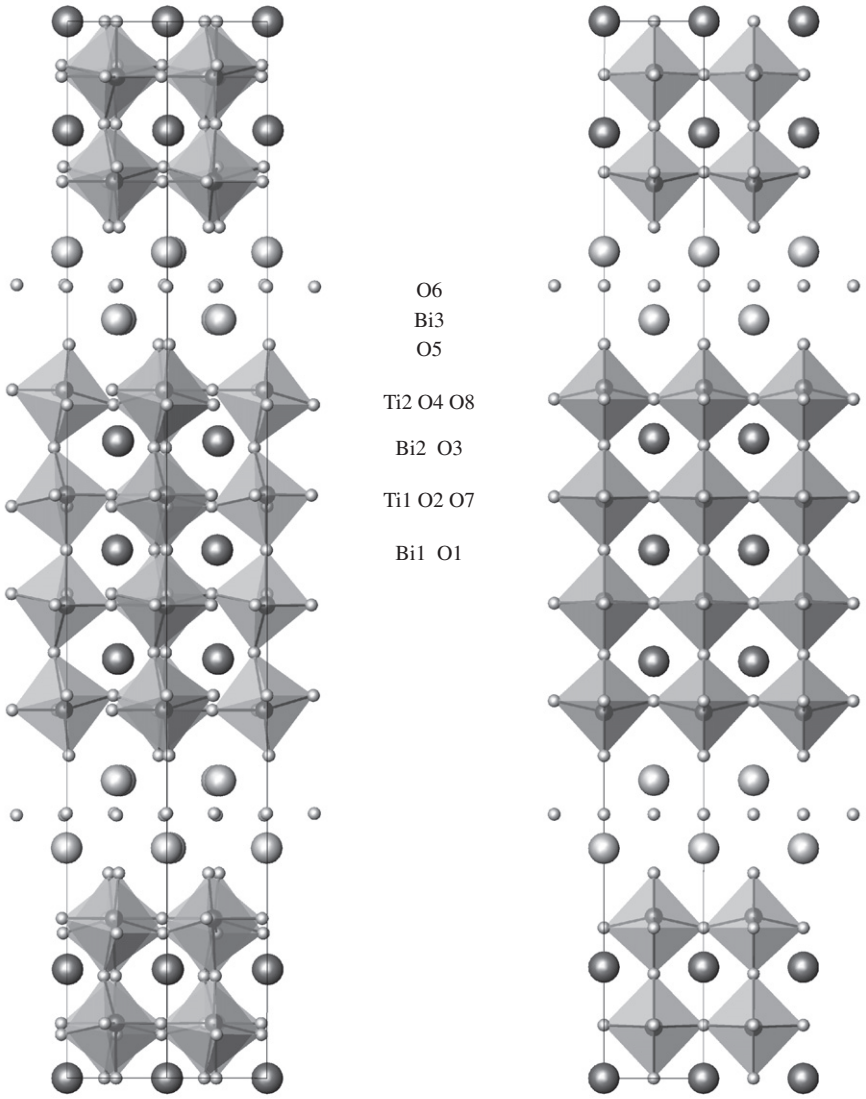

Fig. 7. Structural representations of $Bi_5Ti_3CrO_{15}$: left, at 25 °C, space group $A2_1am$ viewed down [010]; right, at 700 °C, space group $I4/mmm$ viewed down [100]. Large black/grey spheres represent Bi, small black spheres represent Ti, small grey spheres represent O.

shown in Fig. 11. Rietveld analysis of the crystal structure of $Bi_5Ti_3CrO_{15}$ at 700 °C was based on a model in space group $I4/mmm$ (total of 40 variables, with 24 structural parameters). The distribution of Ti/Cr cations over the Ti/Cr1 and Ti/Cr2 sites was maintained at the ratios determined at 25 °C (0.629/0.371 and 0.871/0.129, respectively). The co-ordinates and isotropic thermal parameters of the Ti/Cr cations occupying the same crystallographic site were constrained to be equal. The refinement converged to give satisfactory fits to the diffraction data, as shown in Fig. 12. The final structural and goodness of fit parameters are reported in Table 5, key bond lengths are summarised in Table 6.

4. Discussion

4.1. Room temperature structure

Rietveld analysis of high resolution neutron diffraction data at 25 °C confirmed the $n=4$ Aurivillius phase $Bi_5Ti_3CrO_{15}$ to be isostructural with the known homologues $Bi_4ATi_4O_{15}$ and $Bi_5Ti_3FeO_{15}$ (A=Ba, Sr, Ca, Pb) [37–40]. At room temperature these materials all adopt $A2_1am$ symmetry, which is consistent with the hypothesis of Newnham et al. that polar Aurivillius structures, $Bi_2A_{n-1}B_nO_{3n+3}$, with n=even should adopt space group $A2_1am$, whereas structures with n=odd should adopt space group $B2cb$ [43]. In the aristotype $I4/mmm$ structure with n=even, a mirror plane perpendicular to c, and a 2-fold rotation axis parallel to a, intersect the central plane of apical oxygen atoms in the $[A_{n-1}B_nO_{3n+1}]^{2-}$ perovskite type layer. In the polar $A2_1am$ and $B2cb$ structures, tilting of rigid BO_6 octahedra in the perovskite type layer involves displacement of apical oxygen atoms parallel to the b-axis, leading to loss of the vertical mirror plane, perpendicular to b and formation of a short contact between equatorial apical oxygen atoms and Bi atoms in the $[Bi_2O_2]^{2+}$ layer. Retention of the mirror plane in polar $A2_1am$, permits co-operative rotation of undistorted BO_6 octahedra, whereas retention of the 2-fold axis in $B2cb$ requires distortion of the BO_6 octahedra to achieve co-operative rotation. Thus, strain energy associated with deformation of BO_6 octahedra is minimised in space group $A2_1am$ for polar Aurivillius phases with n=even, as determined for the $n=4$ Aurivillius phases $Bi_4ATi_4O_{15}$, $Bi_5Ti_3FeO_{15}$, and $Bi_5Ti_3CrO_{15}$. In the case of polar Aurivillius phases with

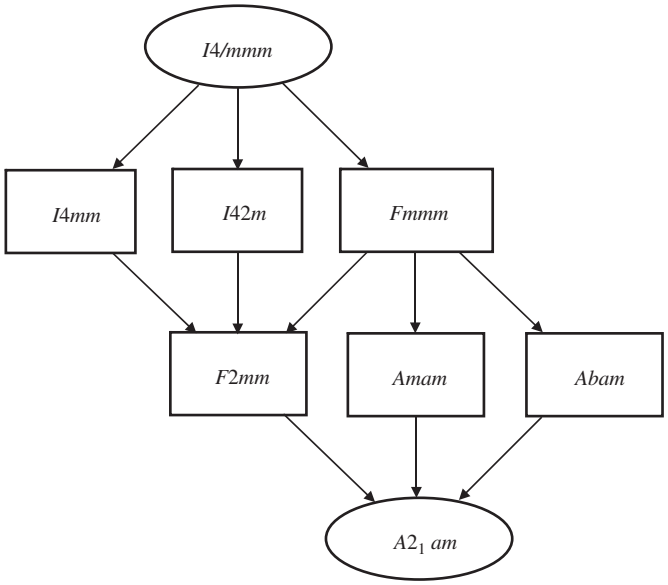

Fig. 8. Group–sub-group relations connecting space groups $I4/mmm$ and $A2_1am$, using common non-standard settings, generated using the program "Subgroupgraph", on the Bilbao Crystallographic Server [42].

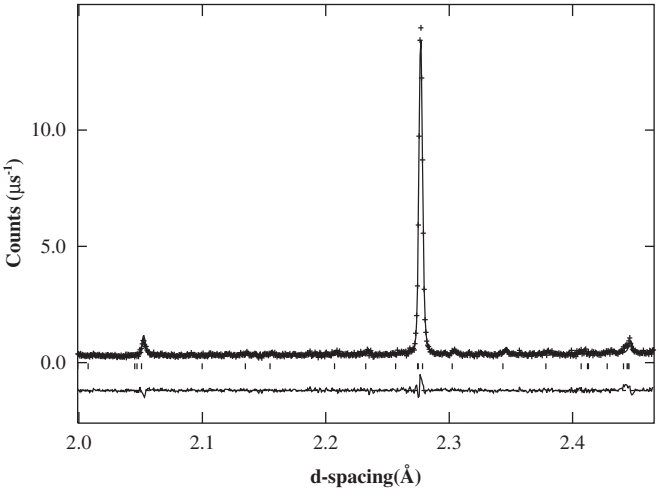

Fig. 9. Showing fit (solid line) to high resolution (Bank 1, $2\theta \approx 168^\circ$) neutron diffraction data (points) for $Bi_5Ti_3CrO_{15}$ at 650 °C in space group $A2_1am$; tick marks show allowed reflections, the difference profile (lower solid line) demonstrates an excellent fit to the data. Note the presence of $h\ k\ l$ reflections with $h+l \neq 2n$ which are permitted by $A2_1am$ but not $F2mm$; e.g. (1 2 8), (1 2 6), (2 1 5) and (1 2 4) reflections, located at $d \approx 2.21$, 2.31, 2.35, and 2.28 Å.

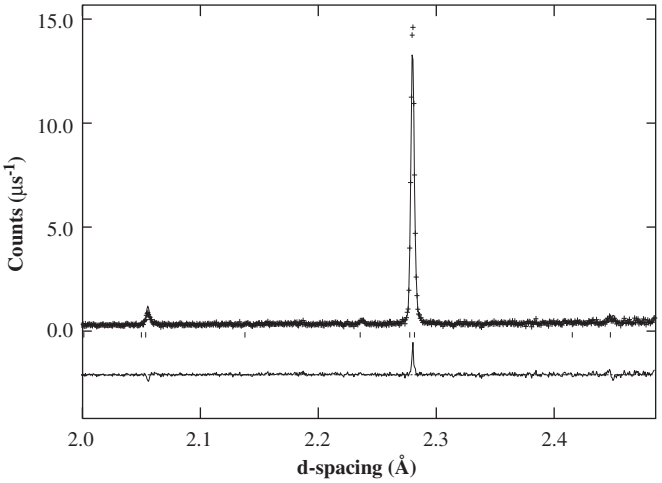

Fig. 10. Showing fit (solid line) to high resolution (Bank 1, $2\theta \approx 168^\circ$) neutron diffraction data (points) for $Bi_5Ti_3CrO_{15}$ at 700 °C, in space group $I4/mmm$; tick marks show allowed reflections, the difference profile (lower solid line) demonstrates an excellent fit to the data. Note absence of $h\ k\ l$ reflections with $h+l \neq 2n$ which are permitted by $A2_1am$, $Amam$ and $Abam$; e.g. (1 2 8), (1 2 6), (2 1 5) and (1 2 4) reflections, located at $d \approx 2.21$, 2.31, 2.35, and 2.28 Å, respectively (compare to Fig. 9).

n=odd, retention of the 2-fold rotation axis permits co-operative rotation of undistorted BO_6 octahedra, whereas, in contrast, retention of the mirror plane requires distortion of the BO_6 octahedra. Thus, for n=even, strain energy is minimised by retention of the 2-fold rotation axis parallel to a in $B2cb$.

As shown in Fig. 7, the Bi cations in the perovskite-type layer of $Bi_5Ti_3CrO_{15}$ adopt distorted dodecahedral co-ordination at 25 °C. The central Bi1 cation is displaced toward one square face forming eight short (2.3–2.6 Å) and four long (3.0–3.2 Å) Bi–O bonds. The outer Bi2 cation is displaced toward a polyhedral edge defined by O3 and O4 atoms, thus forming two short (2.3 Å), four intermediate (2.5–2.8 Å), and six long (3.0–3.2 Å) Bi–O bonds. The bond valence sums for the Bi1 and Bi2 cations are satisfactory but indicate that both Bi cations are slightly under-bonded (Table 4). The Ti/Cr cations adopt distorted octahedral co-ordination in $Bi_5Ti_3CrO_{15}$ at 25 °C, as shown in Fig. 7. The inner Ti/Cr1 cations are displaced toward an octahedral face forming three short (1.8–1.9 Å) and three long (2.1–2.2 Å) Ti/Cr1-O bonds. The outer Ti/Cr2 cations are essentially displaced toward an apical oxygen forming one short (1.76 Å), one long (2.24 Å), and four intermediate (1.92–1.99 Å) Ti/Cr2-O bonds. The bond valence sums calculated for the Ti and Cr cations are satisfactory but show that both are slightly overbonded in the Ti/Cr1 and Ti/Cr2 sites (Table 4). The co-ordination of the Bi3 cation in the $[Bi_2O_2]^{2+}$ layer is essentially a capped square anti-prism, with the Bi3 cation displaced toward a triangular face, forming three short (2.2–2.3 Å), three intermediate (2.5–2.6 Å), and two long (3.1–3.2 Å), Bi–O bonds; plus formation of an additional Bi3-O8 contact of ~3.13 Å to an equatorial oxygen in the perovskite-type layer. The Bi3 cation is only slightly under-bonded in this environment, as demonstrated by the calculated bond valence sum of 2.92 v.u.. The spread of oxygen isotropic thermal parameters reported in Table 2 appears typical of Aurivillius phases with cation disorder on both A- and B-sites of the perovskite type layer (see e.g. [20] and [40]). The larger thermal parameters may relate to small static displacements of these atoms from the refined positions, influenced by cation disorder.

As shown in Fig. 7, the Ti/Cr octahedra in the perovskite-type layer of $Bi_5Ti_3CrO_{15}$ undergo co-operative tilting at room temperature, in order to relieve bond length mismatch. Previous studies of $Bi_2A_2B_3O_{12}$ Aurivillius phases have demonstrated a mismatch in the "ideal" lateral dimensions of the constituent fluorite and perovskite layers: the natural a parameter of the Bi_2O_2 fluorite layer is estimated to be a_f=3.80 Å, with that of the perovskite type layer, a_p, given by the following empirical relation determined by analysis of a wide range of compounds [13,43,44]:

$$a_p = 1.33\,r_B + 0.60\,r_A + 2.36\,\text{Å} \quad (1)$$

where, by convention, r_A and r_B are the (weighted mean) Shannon radii for 6 co-ordinate B and 8-co-ordinate A site cations, respectively [45]. Substitution of r_A=1.20 Å and r_B=0.61 Å, for Bi and Ti/Cr, respectively, yields a_p=3.89 Å for $Bi_5Ti_3CrO_{15}$. Thus, to accommodate the interfacial mismatch between fluorite and perovskite-type layers, the Ti/CrO_6 octahedra undergo co-operative tilting, as shown in Fig. 7, in order to maintain satisfactory Ti/Cr–O bond lengths. The pattern of octahedral tilts in $Bi_5Ti_3CrO_{15}$ is identical to that observed in $Bi_5Ti_3FeO_{15}$ and $Bi_4SrTi_4O_{15}$:

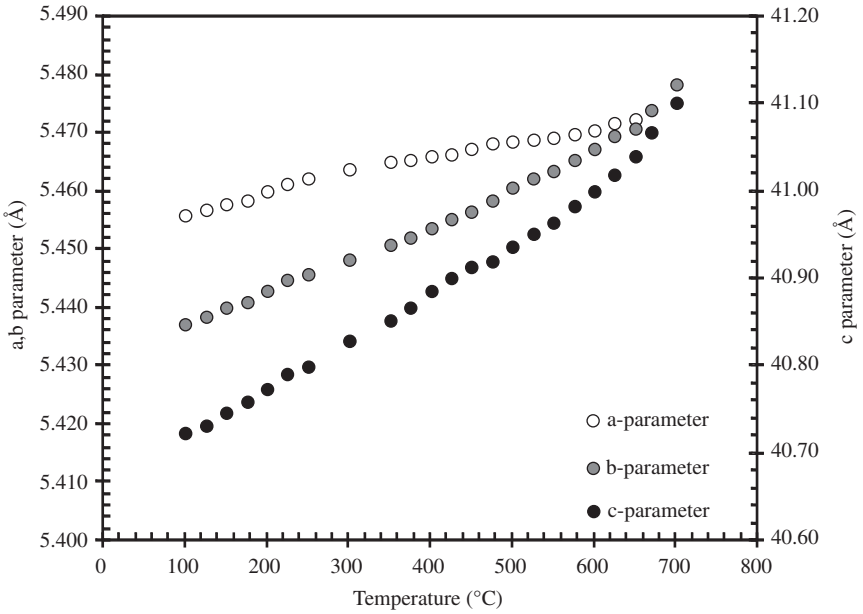

Fig. 11. Temperature dependence of unit cell parameters of $Bi_5Ti_3CrO_{15}$; note $a\sqrt{2}$ is plotted above 660 °C (note: error bars are within size of points).

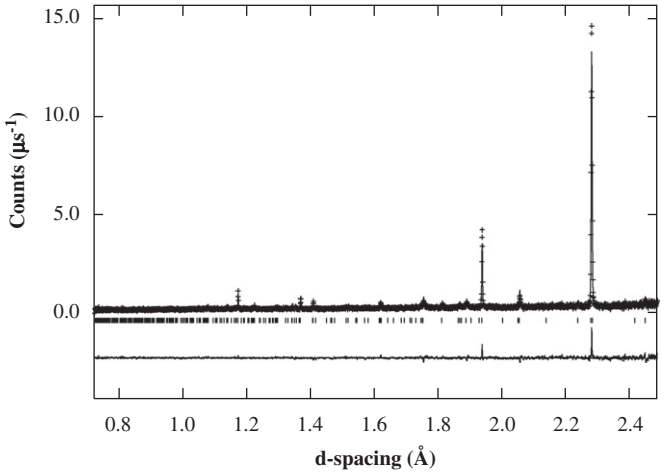

Fig. 12. Showing fit (solid line) to high resolution (Bank 1, $2\theta \approx 168^\circ$) neutron diffraction data (points) for $Bi_5Ti_3CrO_{15}$ at 700 °C in space group *I*4/*mmm*; tick marks show allowed reflections, the difference profile (lower solid line) demonstrates an excellent fit to the data.

Table 5
Refined structural parameters for $Bi_5Ti_3CrO_{15}$ at 700 °C in space group *I*4/*mmm*.

Space group: *I*4/*mmm*		$a=3.873707(35)$ Å	$c=41.1000(8)$ Å		
Atom	**Pos.**	***x***	***y***	***z***	**U_{iso} (× 100) Å²**
Bi1	2*a*	0	0	0	7.4(3)
Bi2	4*e*	0	0	0.1053(2)	8.1(3)
Bi3	4*e*	0	0	0.2177(1)	8.1(2)
Ti/Cr1[a]	4*e*	0	0	0.451(1)	1.3(2)
Ti/Cr2[b]	4*e*	0	0	0.3467(4)	0.70(9)
O1	2*b*	0	0	0.5	8.0(5)
O2	8*g*	0	0.5	0.0503(2)	8.2(2)
O3	4*e*	0	0	0.4009(3)	8.7(4)
O4[c]	8*g*	0	0.5	0.1426(1)	7.8(3)
O5[d]	4*e*	0	0	0.3055(2)	7.8(3)
O6	4*d*	0	0.5	0.25	8.0(4)
	Bank		**R_{wp} (%)**	**R_p (%)**	
Powder statistics	1		12.18	10.14	
	2		8.13	6.46	
	Combined		9.92	7.74	$\chi^2=1.57\%$

[a] Ti/Cr site occupancy fixed at 0.629/0.371 from 25 °C data, co-ordinates and U_{iso} constrained to be equal, site occupancy constrained to unity.
[b] Ti/Cr site occupancy 0.871/0.129 from 25 °C data, co-ordinates and U_{iso} constrained to be equal, site occupancy constrained to unity.
[c] Equivalent to O2 and O7 in $A2_1am$.
[d] Equivalent to O4 and O9 in $A2_1am$.

octahedra rotate *in-phase* parallel to *a*, but *anti-phase* parallel to *b*; whereas, parallel to *c*, pairs of inner/outer octahedra rotate in the *same sense*, but *anti-phase* with respect to each other. That is, parallel to the *c*-axis, the tilt pattern is Ti2(−)–Ti1(+)–Ti1 (+)–Ti2 (−), where (+) and (−) denote, respectively, in-phase and anti-phase rotation.

The spontaneous polarisation, P_s, of $Bi_5Ti_3CrO_{15}$ was estimated by a simple point charge model, with the contribution of each constituent ion to the total spontaneous polarisation given by Eq. (2):

$$P_s = \sum_i \frac{m_i Q_i e \Delta x_i}{V} \quad (2)$$

where m_i is the site multiplicity, Δx_i is the atomic displacement along the *a*-axis from the corresponding position in the parent non-polar *Fmmm* structure, and Q_i is the ionic charge, for each constituent ion, *i*. Based on the refined structural parameters of $Bi_5Ti_3CrO_{15}$ given in Table 2, the calculated spontaneous polarisation at 25 °C is $P_s=34\pm2$ $\mu C\,cm^{-2}$. The individual ion contributions to the spontaneous polarisation are shown in Fig. 13, the most significant contribution to the calculated spontaneous polarisation arises from the shift of the rigid octahedral perovskite framework parallel to the *a*-axis, relative to the stationary Bi1 cation; this is, to some extent, partially cancelled by the opposite displacement of the Ti/Cr atoms.

High temperature neutron diffraction, electrical, and DSC data all point to a high temperature phase transition in $Bi_5Ti_3CrO_{15}$ at 660 °C. If it is assumed this phase transition in $Bi_5Ti_3CrO_{15}$ is associated with a transition between ferroelectric and paraelectric states, then, as shown in Fig. 14, the Curie temperatures of known $n=4$ Aurivillius phases are observed to scale plausibly with the calculated spontaneous polarisation, as would be expected.

Table 6
Bond lengths determined from Rietveld analysis of neutron diffraction data for $Bi_5Ti_3CrO_{15}$ at 700 °C.

Bond (Å)		Bond (Å)	
Bi1–O1	2.73912(2) × 4	Ti/Cr1–O1	1.99(6)
Bi1–O2	2.835(8) × 8	Ti/Cr1–O2	1.9386(28) × 4
		Ti/Cr1–O3	2.08(7)
Bi2–O2	3.977(10) × 4		
Bi2–O3	2.7513(15) × 4	Ti/Cr2–O3	2.228(21)
Bi2–O4	2.470(8) × 4	Ti/Cr2–O4	1.985(4) × 4
		Ti/Cr2–O5	1.690(20)
Bi3–O5	2.904(4) × 4		
Bi3–O6	2.347(4) × 4		

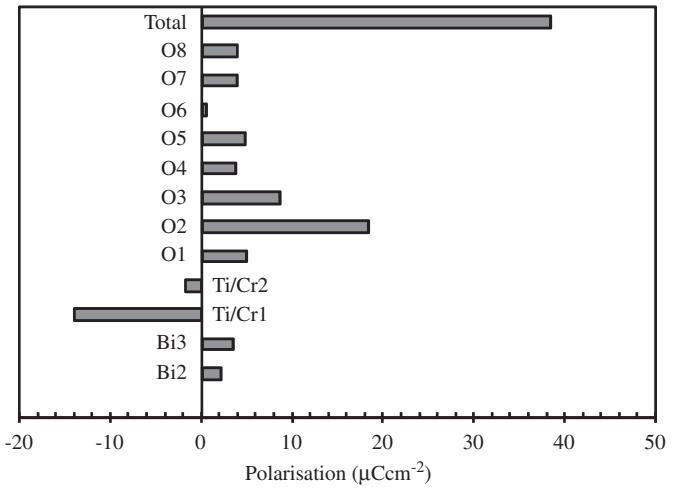

Fig. 13. Contribution to calculated spontaneous polarisation of $Bi_5Ti_3CrO_{15}$ from each constituent ion.

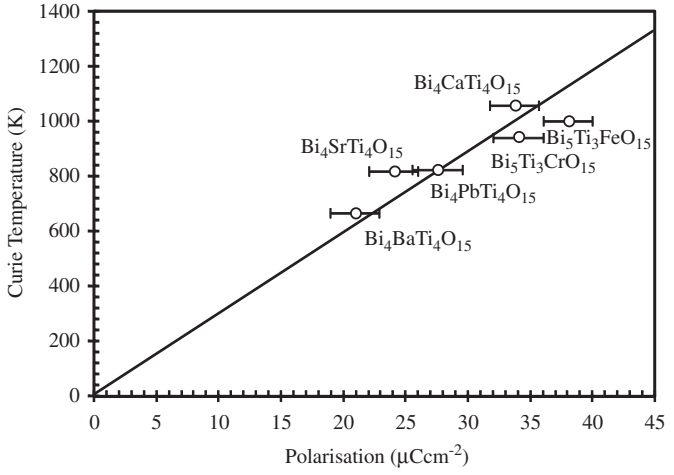

Fig. 14. Correlation of Curie temperature with spontaneous polarisation, calculated by Eq. (2), in $n=4$ Aurivillius phases.

The reasons for successful synthesis of $Bi_5Ti_3MO_{15}$ with M=Cr and Fe, but not M=Mn and Co are unclear. Partial oxidation of Mn^{3+} to Mn^{4+}, as in the case of $Bi_2Sr_{1.4}La_{0.6}NbMn_2O_{12}$ also fabricated in air [19], could explain the failure to synthesise $Bi_5Ti_3MnO_{15}$. A similar redox variation could explain the failure to synthesise $Bi_5Ti_3CoO_{15}$. Alternatively, it has been shown, using calculations based on extended Huckel theory, that distortion of the three dimensional ABO_3 perovskite-type framework becomes increasingly disfavoured for d^n cations with increasing n [46]. This could impose a restriction on the potential d^n transition metal species generally compatible with substitution in the Aurivillius framework to those with $n \leq 5$.

4.2. High temperature structure

The crystal structure of $Bi_5Ti_3CrO_{15}$ adopts the aristotype $I4/mmm$ space group at 670 °C and above, as shown schematically in Fig. 7. In the perovskite type layer, the Bi1 co-ordination polyhedron is a near ideal cuboctahedron, but with a slight axial distortion leading to four short (2.73 Å) and eight longer (2.83 Å) Bi–O bonds. The Bi2 cation is displaced, parallel to the c-axis, within its cuboctahedron leading to four short (2.47 Å), four intermediate (2.75 Å) and four long (3.97 Å) Bi–O bonds. The outer Ti/Cr2 cations are displaced toward one apical oxygen atom of the Ti/CrO_6 octahedra, leading to one short (1.69 Å), one long (2.22 Å), and four intermediate (1.98 Å) Ti/Cr–O bonds. The inner Ti/Cr1 cations adopt an axially distorted octahedral environment with two essentially equivalent apical Ti/Cr–O bonds (2.00 Å), and four equivalent equatorial bonds (1.93 Å). The co-ordination of the Bi3 cation in the $[Bi_2O_2]^{2+}$ layer is a square anti-prism, with the Bi3 cation displaced, parallel to the c-axis, toward a square face forming four short (2.3 Å) and four long (2.90 Å), Bi–O bonds.

4.3. Cation partitioning in the perovskite type layer of $Bi_5Ti_3CrO_{15}$

The contrast in neutron scattering lengths between Ti (−3.438 fm) and Cr (3.635 fm), allows (in principle) accurate determination of the distribution of Ti and Cr over the two unique octahedral sites in the perovskite layer of $Bi_5Ti_3CrO_{15}$. The refined distribution (Table 2), does not lead to null scattering at either cation site, permitting location of the Ti/Cr atoms with reasonable precision. Analysis of neutron diffraction data at 25 °C demonstrated a marked preference of Cr for the inner Ti/Cr1 site, with 74.2% of the Cr atoms partitioning into this site and only 25.8% partitioning into the outer Ti/Cr2 site. At first sight, this distribution appears difficult to rationalise, for two reasons. First, as shown in Table 4, bond valence sums do not indicate a strong preference of Ti/Cr for either site, suggesting that both sites allow reasonable Ti/Cr–O bond lengths to be obtained. Secondly, d^0 cations, such as Ti, generally exhibit a preference for more distorted octahedral sites, stabilised by donation of electron density from filled oxygen 2p states into empty transition metal d^0 states (triggering a second order Jahn Teller distortion). However, at 25 °C, neither the Ti/Cr1 or Ti/Cr2 site is grossly more distorted: this is best quantified by the Shannon site distortion parameter which expresses polyhedral distortion as the distribution of bond lengths about the mean [45], viz

$$\Delta_n = \frac{1}{n}\sum_i \left(\frac{r_i - r_m}{r_m}\right)^2 \times 10^3 \quad (3)$$

where r_i and r_m are individual and average bond lengths in the n-fold co-ordinate polyhedron, respectively. Calculation yields Δ_6=5.6 for the Ti/Cr1 site, and Δ_6=5.2 for the Ti/Cr2 site at 25 °C, compared to Δ_6=0.16 for an essentially regular CrO_6 octahedron in Cr_2O_3 [35].

To rationalise the observed Ti/Cr distribution, we reconsider the high temperature crystal structure of $Bi_5Ti_3CrO_{15}$ in the aristotype $I4/mmm$ space group. At 700 °C, the Shannon site distortion parameter for the inner Ti/Cr1 is Δ_6=0.75, compared to Δ_6=6.17 for the outer Ti/Cr2 site; consistent with the structural description given above. Therefore, a plausible explanation for the observed Ti/Cr distribution is the preference of Ti for the more distorted Ti/Cr2 site during high temperature synthesis, stabilised

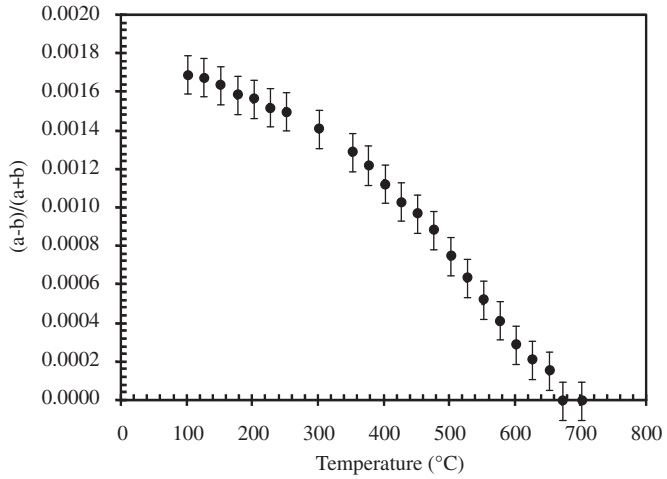

Fig. 15. Temperature dependence of the orthorhombic strain of $Bi_5Ti_3CrO_{15}$.

by the second order Jahn Teller effect, with Cr preferentially occupying the less distorted Ti/Cr1 site.

Electrostatic considerations also favour preferential occupancy of the inner Ti/Cr1 and outer Ti/Cr2 sites by Cr and Ti, respectively. The more highly charged Ti^{4+} species would be expected to occupy the outer Ti/Cr2 site to maximise electrostatic interaction with the layer of oxygen anions in the fluorite layer. This was demonstrated by Madelung energy calculations for the following configurations, based on the scheme of Weenk and Harwig [47]:

(i) Cr totally in outer Ti/Cr2 site: 81,958 kJ mol^{-1}
(ii) Random Cr distribution over both sites: 83,083 kJ mol^{-1}
(iii) Cr totally in inner Ti/Cr1 site: 83,931 kJ mol^{-1}.

Thus, preferential Ti^{4+} occupancy of the outer Ti/Cr2 site, and hence Cr^{3+} occupancy of the inner Ti/Cr1 site, is clearly favoured on electrostatic grounds.

Our evidence for partial cation ordering of Ti/Cr in the perovskite-type layer of $Bi_5Ti_3CrO_{15}$ is in contrast to the random distribution of Ti/Fe in $Bi_5Ti_3FeO_{15}$, determined by a combination of Mossbauer spectroscopy and neutron diffraction [40]. It is uncertain as to whether this difference in behaviour is a consequence of different specific preparation conditions or reflects an underlying subtle difference in crystal chemistry. In the present case, the long schedule of high temperature anneals, with controlled slow cooling rate, could be expected to yield a cation distribution approaching equilibrium. Further investigation of this issue would be of interest, since controlling the distribution of transition metal cations with empty and partially filled *d* states is key to optimization of ferroelectric and magnetic ordering.

4.4. Nature of the high temperature phase transition in $Bi_5Ti_3CrO_{15}$

The temperature dependence of the unit cell parameters and orthorhombic strain of $Bi_5Ti_3CrO_{15}$ are shown in Figs. 11 and 15, respectively. The *a* and *b* parameters show a convergence in the region of the phase transition at 660 °C, coincident with a change in slope of the *c*-axis, as shown in Fig. 11. Interestingly, the orthorhombic strain of $Bi_5Ti_3CrO_{15}$ appears to show a discontinuity at the phase transition, as shown in Fig. 15. As discussed previously, the high temperature neutron diffraction data of $Bi_5Ti_3CrO_{15}$ are well fitted in the centrosymmetric *I*4/*mmm* aristotype space group at 670 °C and above. Therefore, on the basis of the available data we conclude that $Bi_5Ti_3CrO_{15}$ transforms *directly* from $A2_1am$ to *I*4/*mmm* at 660 °C, with no evidence for an intermediate non-polar orthorhombic structure. This behaviour is analogous to that of the known ferroelectric Aurivillius phase $Bi_5Ti_3FeO_{15}$. In contrast, $Bi_4SrTi_4O_{15}$ has been demonstrated to undergo a series of continuous phase transitions from $A2_1am$ to *Amam* at ~550 °C, and *Amam* to *I*4/*mmm* at ~650 °C, with loss of polar displacements but retention of octahedral tilting in the *Amam* intermediate phase [40].

Hyatt et al. [48] rationalised the observation of continuous and discontinuous phase transitions in $n=2$ Aurivillius phases on the basis of crystal chemical arguments. In general, Aurivillius phases with high T_c exhibit a discontinuous $A2_1am \rightarrow I4/mmm$ phase transition, since, at T_c, thermal expansion is sufficient to relieve interfacial bond length mismatch and co-operative octahedral tilting is lost simultaneously. In contrast, Aurivillius phases with low T_c show a sequence of continuous phase transitions, $A2_1am \rightarrow Amam \rightarrow I4/mmm$, since thermal expansion is insufficient to relieve interfacial bond-length mismatch at T_c: co-operative octahedral tilting therefore persists within the temperature window of the *Amam* phase. Taking the room temperature orthorhombic strain as a measure of interfacial bond length mismatch (Fig. 16) (adapted from [48]), shows that temperature for transition to the aristotype *I*4/*mmm* structure scales with the orthorhombic strain (solid line). The temperature stability window of the intermediate *Amam* phase is then determined by the Curie temperature: it is significant for materials with low T_c but disappears altogether for materials with high T_c, as shown by the broken line. In addition to the data plotted by Hyatt et al. for $n=2$ Aurivillius phases, Fig. 16 shows data for the $n=4$ phases $Bi_5Ti_3CrO_{15}$, $Bi_5Ti_3FeO_{15}$, and $Bi_4SrTi_4O_{15}$, for which unambiguous evidence from neutron powder diffraction data permitted the identification or absence of an *Amam* intermediate phase. The observation of a continuous phase transition for $BiSrTi_4O_{15}$, but a discontinuous phase transition in the case of $Bi_5Ti_3CrO_{15}$ and $Bi_5Ti_3FeO_{15}$ is therefore rationalised on the basis of the arguments discussed above. The fact that the stability window of the *Amam* phase scales with room temperature orthorhombic strain and Curie temperature for both $n=2$ and 4 Aurivillius phases, is consistent with the idea that common crystal chemical

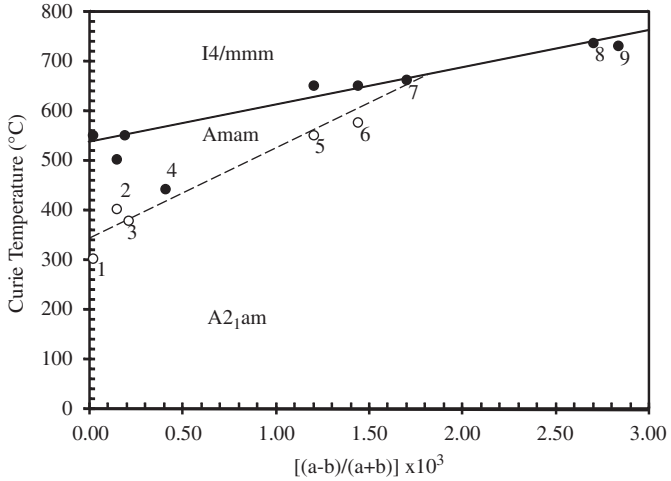

Fig. 16. Structure field map for $n=2$ and 4 Aurivillius phases, showing the stability window of the *Amam* phase defined by the dependence on room temperature orthorhombic strain of the Curie temperature (closed circles) and temperature for transformation to the *I*4/*mmm* aristotype. Data points represent: (1) $Bi_2PbTa_2O_9$, (2) $Bi_2PbNb_2O_9$, (3) $Bi_{2.1}Sr_{0.85}Ta_2O_9$, (4) $Bi_2SrTa_2O_9$, (5) $Bi_4SrTi_4O_{15}$, (6) $Bi_2SrNb_2O_9$, (7) $Bi_5Ti_3CrO_{15}$, (8) $Bi_5Ti_3FeO_{15}$, (9) $Bi_3Ti_{1.5}W_{0.5}O_9$. For $Bi_2SrTa_2O_9$, $Bi_5Ti_3CrO_{15}$ (assuming $T_c=660$ °C), $Bi_5Ti_3FeO_{15}$, and $Bi_3Ti_{1.5}W_{0.5}O_9$, direct transformation from $A2_1am$ to *I*4/*mmm* occurs at the Curie temperature. Lines are drawn to guide the eye.

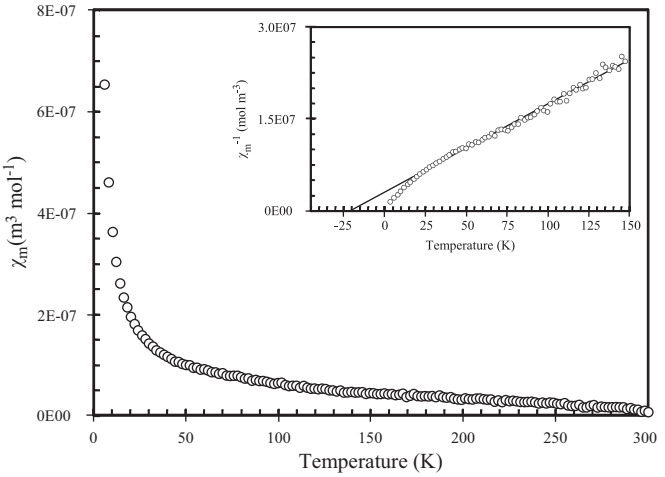

Fig. 17. Field cooled (FC) molar susceptibility, χ_m, as a function of temperature to 3 K. Inset shows inverse molar susceptibility, with dotted line indicating extrapolation to $\theta = -25$ K, suggestive of antiferromagnetic coupling.

parameters control the sequence of phase transitions in this class of materials.

4.5. Magnetic susceptibility

Fig. 17 shows the temperature dependence of the magnetic susceptibility of $Bi_5Ti_3CrO_{15}$, after diamagnetic correction. The compound is found to exhibit paramagnetic behaviour with no evidence for magnetic ordering at low temperature. Fitting the Curie–Weiss Law to the inverse susceptibility below 150 K, yields a Weiss constant of -25 K, demonstrating predominant antiferromagnetic interactions between Cr^{3+} moments, as expected for 180° superexchange interactions between d^3 species [49]. The calculated magnetic moment per formula unit was 1.82(5) μ_B, which is slightly lower than the expected spin only magnetic moment of 1.94 μ_B for Cr^{3+}. This could be explained by local antiferromagnetic coupling of Cr^{3+} magnetic moments, distributed over the two unique octahedral sites, consistent with the negative Weiss constant. Further investigation of the magnetic behaviour of $Bi_5Ti_3CrO_{15}$, and potential dependence on Ti/Cr ordering, would be useful. On the basis of the present data we conclude that long range ordering of magnetic moments does not occur in $Bi_5Ti_3CrO_{15}$ at low temperature. We note that the observed paramagnetic behaviour of $Bi_5Ti_3CrO_{15}$ with short range antiferromagnetic interactions is similar to that recently reported by Dong et al. [16] for isostructural $Bi_5Ti_3FeO_{15}$.

5. Conclusions

The $n=4$ Aurivillius phase, $Bi_5Ti_3CrO_{15}$, was synthesised and characterised. The compound adopts the polar space group $A2_1am$ at room temperature and transforms directly from $A2_1am$ to $I4/mmm$ above 660 °C, with no evidence for any intermediate phase below or above this transition temperature (within the temperature resolution of our data: 10 °C). This phase transition is accompanied by a maximum in relative permittivity and divergence of loss tangent, characteristic (but not definitive) of a transformation between ferroelectric and paraelectric states. $Bi_5Ti_3CrO_{15}$ exhibits paramagnetic behaviour at low temperature, with short range antiferromagnetic interactions, but no evidence for long range magnetic ordering. Neutron diffraction demonstrated partial ordering of Ti/Cr over the available octahedral sites in the perovskite-type layer of $Bi_5Ti_3CrO_{15}$, apparently driven by the preference of the Ti^{4+} cation for the more distorted octahedral site during high temperature synthesis, based on electrostatic considerations. The presence of Cr^{3+} in the anticipated oxidation state was confirmed by analysis of Cr K-edge XANES. Disorder of Cr^{3+} cations is considered to result in short range antiferromagnetic coupling of magnetic moments, possibly in local clusters, inhibiting long range magnetic ordering. This study has demonstrated the potential for at least partial ordering of transition metal cations with partially filled d states in $n=4$ Aurivillius phases, whilst maintaining polar displacements. However, discovery of new multiferroics in this class of materials will likely require more ordered and concentrated substitution of species with partially filled d states.

Acknowledgments

We thank EPSRC for support of a studentship to A.T.G., and EPSRC and NDA for support of a studentship to D.R.P. Experiments at the ISIS Pulsed Neutron and Muon Source were supported by a beamtime allocation from the Science and Technology Facilities Council. We are grateful to Dr. Kevin Knight for assistance in acquisition of neutron diffraction data. Use of the National Synchrotron Light Source, Brookhaven National Laboratory, was supported by the US Department of Energy, Office of Science, Office of Basic Energy Sciences, under Contract no. DE-AC02-98CH10886. We are grateful to the five anonymous reviewers for their careful consideration of our draft manuscript and suggestions for improvement.

References

[1] N.A. Hill, J. Phys. Chem. B 104 (2000) 6694.
[2] N.A. Hill, J. Magn. Magn. Mater. 242 (2002) 976.
[3] I. Sosnowska, T.P. Neumaier, E. Steichele, J. Phys. C 15 (1982) 4835.
[4] A. Belik, S. Iitubo, K. Kodama, N. Igawi, S. Shamoto, E. Takayama-Muromachi, Chem. Mater. 18 (2006) 798.
[5] A. Belik, S. Iitubo, K. Kodama, N. Igawi, S. Shamoto, E. Takayama-Muromachi, Chem. Mater. 20 (2008) 3765.
[6] S. Niitaka, M. Azuma, M. Takano, E. Nishibori, M. Takata, M. Sakata, Solid State Ionics 172 (2004) 557.
[7] S.M. Selbach, M.A. Einarsrud, T. Grande, Chem. Mater. 21 (2009) 169.
[8] A. Aurivillius, Ark. Chem. 1 (1949) 499.
[9] G.A. Smolenskii, V.A. Isupov, A.I. Agranovskaya, Sov. Phys. Solid State 3 (1959) 651.
[10] E.C. Subbarao, J. Phys. Chem. Solids 23 (1962) 665.
[11] N.A. McDowell, K.S. Knight, P. Lightfoot, Chem. Eur. J. 12 (2006) 1493.
[12] S.M. Blake, M.J. Falconer, M. McCreedy, P. Lightfoot, J. Mater. Chem. 7 (1997) 1609.
[13] C. Hervoches, P. Lightfoot, Chem. Mater. 11 (1999) 3359.
[14] A. Snedden, C. Hervoches, P. Lightfoot, Phys. Rev. B 67 (2003) 092102.
[15] X.Y. Mao, W. Wang, X. Chen, Solid State Commun. 147 (2008) 186.
[16] X.W. Dong, K.F. Wang, J.G. Wan, J.S. Zhu, J. Liu, J. Appl. Phys. 103 (2008) 094101.
[17] A. Srinivas, S.V. Suryanarayana, G.S. Kumar, M.M. Kumar, J. Phys.: Condens. Matter 11 (1999) 3335.
[18] G. Ismailzade, V.I. Nesterenko, F.A. Mirshili, P.A. Rustamov, Sov. Phys. Crystallogr. 12 (1967) 400.
[19] E.E. McCabe, C. Greaves, J. Mater. Chem. 15 (2005) 177.
[20] E.E. McCabe, C. Greaves, J. Solid State Chem. 181 (2008) 3051.
[21] N. Sharma, C.D. Ling, G.E. Wrighter, P.Y. Chen, B.J. Kennedy, P.L. Lee, J. Solid State Chem. 180 (2007) 370.
[22] N. Sharma, B.J. Kennedy, M.M. Elcombe, Y. Liu, C.D. Ling, J. Phys.: Condens. Matter 20 (2008) 025215.
[23] M. Lufaso, W. Schulze, S. Misture, T. Vanderah, J. Solid State Chem. 180 (2007) 2655.
[24] B. Ravel, M. Newville, J. Synchrotron Radiat. 12 (2005) 537.
[25] A.C. Larson, R.B. von Dreele, General Structure Analysis System (GSAS), Los Alamos National Laboratory, New Mexico, 2004.
[26] D.Y. Suárez, I.M. Reaney, W.E. Lee, J. Mater. Res. 16 (2001) 11.
[27] J. Yin, Q. He, Y.N. Huang, X.Y. Huang, X.Y. Chen, Z.G. Liu, Phys. Stat. Sol. 168 (1998) 519.
[28] S.R. Sutton, K.W. Jones, B. Gordon, M.L. Rivers, S. Bajt, J.V. Smith, Geochim. Cosmochim. Acta 57 (1993) 461.
[29] M.D. Szulczewski, P.A. Helmke, W.F. Bleam, Environ. Sci. Technol. 31 (1997) 2954.

[30] K.M. Kemner, Science 306 (2004) 686.
[31] M. Tromp, J. Moulin, G. Reid, J. Evans, AIP Conf. Proc. 882 (2007) 699.
[32] I. Arcon, B. Mirtic, A. Kodre, J. Am. Ceram. Soc. 81 (1998) 222.
[33] A. Pantelouris, H. Modrow, M. Pantelouris, J. Hormes, D. Reinen, Chem. Phys. 300 (2004) 13.
[34] A. Bianconi, E. Fritsch, G. Calas, J. Petiau, Phys. Rev. B 32 (1985) 4292.
[35] R.E. Newnham, Y.M. de Haan, Am. Mineral. 43 (1958) 1098.
[36] T.J. Swoboda, P. Arthur, N.L. Cox, J.N. Ingraham, A.L. Oppegard, M.S. Sadler, J. Appl. Phys. 32 (1961) 374.
[37] B.J. Kennedy, Y. Kubota, B.A. Hunter, K.Kato Ismunandar, Solid State Commun. 126 (2003) 653.
[38] B.J. Kennedy, Q. Zhou, Y. Ismunandar, K.Kato Kubota, J. Solid State Chem. 181 (2008) 1377.
[39] J. Tellier, P. Boullay, M. Manier, D. Mercurio, J. Solid State Chem. 177 (2004) 1829.
[40] C.H. Hervoches, A. Snedden, R. Riggs, S.H. Kilcoyne, P. Manuel, P. Lightfoot, J. Solid State Chem. 164 (2002) 280.
[41] I.D. Brown, D. Altermatt, Acta Crystallogr. B41 (1985) 244.
[42] S. Ivantchev, E. Kroumova, G. Madariaga, J. Perez-Mato, M. Aroyo, J. Appl. Crystallogr. 33 (2000) 1190.
[43] R.E. Newnham, R.W. Wolfe, J.F. Dorrain, Mater. Res. Bull. 6 (1971) 1029.
[44] N.C. Hyatt, J.A. Hriljac, T.P. Comyn, Mater. Res. Bull. 38 (2003) 837.
[45] R.D. Shannon, Acta Crystallogr. A32 (1976) 751.
[46] R.A. Wheeler, M. Whangbo, T. Hughbanks, R. Hoffman, J.H. Burdett, T. Albright., J. Am. Chem. Soc. 108 (1986) 2222–2236.
[47] J.W. Weenk, H.A. Harwig, J. Phys. Chem. Solids 38 (1977) 1047.
[48] N.C. Hyatt, I.M. Reaney, K.S. Knight, Phys. Rev. B 71 (2005) 024119.
[49] J.B. Goodenough, Magnetism and the Chemical Bond, Interscience Publishers, New York, 1963.